IEEE Access
Multidisciplinary | Rapid Review | Open Access Journal

Received July 1, 2019, accepted July 18, 2019, date of publication July 29, 2019, date of current version August 14, 2019.

Digital Object Identifier 10.1109/ACCESS.2019.2931734

Disturbance Observer-Based Adaptive Current Control With Self-Learning Ability to Improve the Grid-Injected Current for *LCL*-Filtered Grid-Connected Inverter

JIAHAO LIU[1], WEIMIN WU[1], (Member, IEEE), HENRY SHU-HUNG CHUNG[2], (Fellow, IEEE), AND FREDE BLAABJERG[3], (Fellow, IEEE)

[1]Department of Electronic Engineering, Shanghai Maritime University, Shanghai 201306, China
[2]Department of Electronic Engineering, City University of Hong Kong, Hong Kong
[3]Department of Energy Technology, Aalborg University, DK-9220 Aalborg, Denmark

Corresponding author: Weimin Wu (wmwu@shmtu.edu.cn)

This work was supported in part by the National Natural Science Foundation of China (NSFC) under Grant 51577114, in part by the NSFC under Grant 51877130, in part by the Shanghai Municipal Education Committee under Grant 14SG43, and in part by the Shanghai Science and Technology Commission under Grant 17040501500.

ABSTRACT During the design of the conventional current controller for a grid-connected inverter with *LCL* filter, the parameter mismatches and disturbances are generally neglected, which may seriously affect the control performance, even result in instability. In order to improve the ability of disturbance rejection and ensure a desired control performance, this paper proposes an Adaptive PID (APID) controller with the self-learning ability based on the Disturbance Observer (DOB). First, the full state-feedback and state observer are utilized to achieve active damping and eliminate the effect of computational delay. Then, aiming to estimate and compensate the lumped disturbance, a DOB is designed. Beneficial from DOB, the steady-state performance is almost not affected by model uncertainties and unmodeled dynamics, however, the transient performance is still deteriorated inevitably due to the limitation of DOB. Thus, an online adaptive method using APID is finally proposed to further improve grid-injected current dynamics. The control parameters can be automatically adjusted in real time by adaptive learning rule, which significantly improves the system robustness and the control performance. Simulation and experiments are provided to demonstrate the effectiveness of the proposed strategy.

INDEX TERMS Adaptive PID controller, disturbance observer, full state-feedback, LCL filter, state observer.

I. INTRODUCTION

The *LCL* filter has been widely adopted in grid-connected inverters since they can provide improved attenuation on the pulse width modulation switching harmonics compared with the *L* filter [1], which allows the use of smaller inductance to satisfy the stringent harmonic requirements [2], [3]. In order to achieve excellent performances and address global stability, various control strategies have been proposed, such as PI-based control [4], [5], Repetitive Control (RC) [6], [7], Sliding Mode Control (SMC) [8], [9], Deadbeat Control (DBC) [10], [11], Model Predictive Control (MPC) [12], [13], etc. Most of the aforementioned methods are model-based control scheme, thus the grid-injected current is sensitive to the uncertainties, which means the unmodeled dynamics and disturbances of inverters, including nonlinear load, parameter uncertainties, grid inductance variation [14], dead time, on-state voltage drop of switching devices and diodes, would inevitably cause performance deterioration.

To eliminate the influence of disturbances, several Disturbance/Uncertainty Estimation and Attenuation (DUEA) schemes had been proposed [15]. Recently, DUEA schemes on the grid-connected inverters, such as Uncertainty

The associate editor coordinating the review of this manuscript and approving it for publication was Snehal Gawande.

and Disturbance Estimator (UDE) [16], Extended State Observer (ESO) [17], Active Disturbance Rejection Control (ADRC) [18] and DOB [19], have become a research hotspot. In [16], a UDE-based grid-injected current control strategy was proposed. This method allows decoupling between disturbance attenuation and reference tracking, however, the introduced differential feedforward may be sensitive to noise. Wang *et al.* [17] separated observation dynamics and parameter mismatches error by utilizing ESO, which can guarantee robust adaption for parameter variation. Nevertheless, the method is only applicable for constant or slowly varying disturbance estimation. Benrabah *et al.* [18] presented a simplified robust control method based on ADRC [20] using Padé approximation. In this strategy, the first order linear ADRC controller is applied to deal with parameter variation of *LCL* filter, which greatly simplifies the controller design, yet brings adverse effects into the closed-loop control performances. In [19], DOB-based feedforward scheme was proposed by introducing the estimation of fluctuations into the reference of the inner loop, which can remarkably attenuate disturbance effects both in structure and external power.

Among these DUEA strategies above, owing to its relatively simple structure and prominent performance [21]–[23], DOB, combining with other controller, is increasingly adopted in the applications of inverters to improve the ability of disturbance rejection. In [24], PI controller based on feedback linearization technique and DOB, was proposed to provide good steady-state performance and improve robustness. However, its assumption that the lumped disturbance approaches to constant value may be not satisfied sometimes, especially when the background harmonic voltage exists. In [25], an internal model-based DOB was proposed to enhance the control performance. This controller fuses the merits of DOB and RC. Nevertheless, the tracking characteristic and stability are affected by the time delay element introduced by RC. Nguyen and Jung [26] investigated a DOB-based MPC, achieving fast dynamic response under the uncertain parameters. However, the unconstrained mode and constrained mode bring high computational effort.

It should be pointed out that although the steady-state performance is almost not be affected by model uncertainties or unmodeled dynamics under the contribution of DOB, the transient performance is still deteriorated inevitably. Because the model uncertainties and external disturbances cannot be completely eliminated due to limitation of DOB [25], and they will produce a transient component to the grid-injected current, which will degrade transient performance. However, few studies on DOB-based control of the grid-connected inverters have considered this issue so far. Aiming to overcome it and further improve grid-injected current dynamics, an effective way is to integrate online adaptive method into the designed controller [22], [27]. For example, in [28], DOB-based fuzzy SMC strategy was proposed. The switching gain can be adaptively adjusted, which achieves strong robustness and fast response. However, it only compensates constant or slowly varying disturbance.

Motivated by the aforementioned limitations, this paper proposes an Adaptive PID (APID) controller with the self-learning ability based on DOB. Firstly, the full state-feedback which plays a role of the active damping is utilized. It is well known that this feedback strategy can arbitrarily assign the position of the closed-loop poles, which can obtain the desired dynamic response [29]. While, since more sensors are required, a state observer is also constructed as a state predictor to reduce the number of sensors and eliminate the influence of computational delay. Secondly, aiming to compensate the lumped disturbance and relax the sensitivity issue, a DOB is designed. DOB possesses two-degrees-of-freedom structure, allowing to decouple the tracking performance and disturbance rejection by the independent design of nominal controller and DOB. Therefore, the excellent tracking performance and disturbance rejection can be achieved simultaneously. Finally, an adaptive PID regulator with the self-learning ability is proposed to prevent transient performance deterioration. The control parameters can be automatically adjusted in real time by adaptive learning rule, which further improves the system robustness and the control performance.

The rest of this paper is organized as follows. The modeling of three-phase grid-connected voltage-source inverter with *LCL* filter is provided in Section II. Then, in Section III, the theoretical analysis and design of the proposed strategy are addressed. The robust stability under model uncertainties is analyzed based on the small-gain theorem in Section IV. The effectiveness of the proposed method is demonstrated by a series of comparative simulations and experiments in Section V. Finally, a conclusion of the paper is drawn in Section VI.

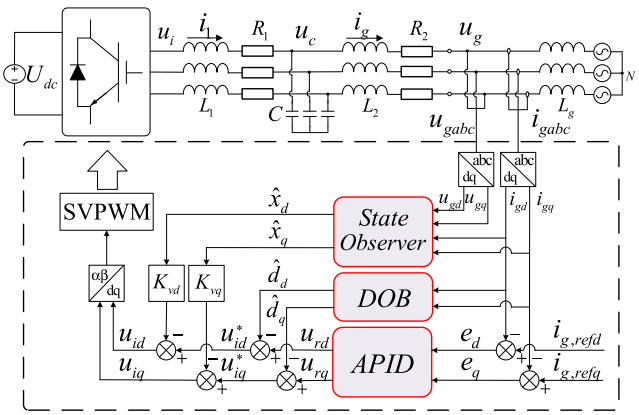

FIGURE 1. The proposed control scheme.

II. MODELING OF GRID-CONNECTED VOLTAGE SOURCE INVERTER WITH LCL FILTER

A three-phase grid-connected voltage-source inverter with *LCL* filter is depicted in Fig. 1. Inverter-side inductor L_1, filter

capacitor C and grid-side inductor L_2 give the LCL filter. L_g is the equivalent grid inductor. R_1, R_2 are the equivalent series resistances of L_1 and L_2, respectively. U_{dc}, u_i and u_g represent the DC-link, inverter output and the Point of Common Coupling (PCC) voltages, respectively. The state vector is selected as $x = \left[i_1, u_c, i_g\right]^T$, where u_c is the filter capacitor voltage, i_1 and i_g are the inverter-side and grid-injected currents, respectively.

Thus, in the synchronous reference frame rotating at the grid angular frequency ω_g, the state-space equation is expressed as:

$$\begin{cases} \dot{x} = \tilde{A}x + B_1 u_i + B_2 u_g \\ y = C_c x \end{cases} \tag{1}$$

where

$$\tilde{A} = \begin{bmatrix} -\frac{R_1}{L_1} - j\omega_g & -\frac{1}{L_1} & 0 \\ \frac{1}{C} & -j\omega_g & -\frac{1}{C} \\ 0 & \frac{1}{L_2} & -\frac{R_2}{L_2} - j\omega_g \end{bmatrix},$$

$$B_1 = \begin{bmatrix} \frac{1}{L_1} & 0 & 0 \end{bmatrix}^T,$$

$$B_2 = \begin{bmatrix} 0 & 0 & -\frac{1}{L_2} \end{bmatrix}^T, \quad \text{and } C_c = \begin{bmatrix} 0 & 0 & 1 \end{bmatrix}.$$

Due to the coupling terms between d- and q-axis, it is complicated to design a desired controller. In this paper, the coupling terms are treated as a part of internal disturbances, since they have a negligible influence on the stability of system, if the controller parameters are well tuned. And taken the parameter mismatches and unmodeled dynamics into consideration, the model is rewritten as:

$$\begin{cases} \dot{x}_d = Ax_d + B_1 u_{id} + B_2 u_{gd} + \Phi\lambda_d \\ y_d = C_c x_d \end{cases}$$
$$\begin{cases} \dot{x}_q = Ax_q + B_1 u_{iq} + B_2 u_{gq} + \Phi\lambda_q \\ y_q = C_c x_q \end{cases} \tag{2}$$

where

$$A = \begin{bmatrix} -\frac{R_1}{L_1} & -\frac{1}{L_1} & 0 \\ \frac{1}{C} & 0 & -\frac{1}{C} \\ 0 & \frac{1}{L_2} & -\frac{R_2}{L_2} \end{bmatrix}, \quad \text{and}$$

$$\Phi = \begin{bmatrix} -\frac{1}{L_1} & 0 & 0 \\ 0 & -\frac{1}{C} & 0 \\ 0 & 0 & -\frac{1}{L_2} \end{bmatrix}.$$

The subscript d and q are the component of d- and q- axis, respectively. λ_d and λ_q represent the lumped disturbance caused by the parameter variations, cross-coupling and other unstructured uncertainties, which can be deduced as:

$$\begin{cases} \lambda_d = \begin{bmatrix} \Delta L_1 i_{1d} - L_1\omega_g i_{1q} - \Delta L_1\omega_g i_{1q} + \Delta R_1 i_{1d} + \varepsilon_{1d} \\ \Delta C\dot{u}_{cd} - C\omega_g u_{cq} - \Delta C\omega_g u_{cq} + \varepsilon_{2d} \\ \Delta L_2 i_{gd} - L_2\omega_g i_{gq} - \Delta L_2\omega_g i_{gq} + \Delta R_2 i_{gd} + \varepsilon_{3d} \end{bmatrix} \\ \lambda_q = \begin{bmatrix} \Delta L_1\dot{i}_{1q} + L_1\omega_g i_{1d} + \Delta L_1\omega_g i_{1d} + \Delta R_1 i_{1q} + \varepsilon_{1q} \\ \Delta C\dot{u}_{cq} + C\omega_g u_{cd} + \Delta C\omega_g u_{cd} + \varepsilon_{2q} \\ \Delta L_2 i_{gq} + L_2\omega_g i_{gd} + \Delta L_2\omega_g i_{gd} + \Delta R_2 i_{gq} + \varepsilon_{3q} \end{bmatrix} \end{cases} \tag{3}$$

where the symbol "Δ" denotes the deviation from the nominal values, ε_d and ε_q represent the unmodeled uncertainties of d- and q-axis, respectively.

Obviously, the expressions in the d- and q-axis are identical, in essence. Hereafter, for the brevity of notation, the subscript d and q will be omitted.

For digital implementation of the control algorithm, the state space equation is represented in discrete-time domain as follows:

$$\begin{cases} x(k+1) = Gx(k) + H_1 u_i(k) + H_2 u_g(k) + \Gamma\lambda(k) \\ y(k) = C_c x(k) \end{cases} \tag{4}$$

where

$$G = e^{AT_s}, \quad H_1 = \int_0^{T_s} e^{A\tau} d\tau B_1,$$
$$H_2 = \int_0^{T_s} e^{A\tau} d\tau B_2, \quad \Gamma = \int_0^{T_s} e^{A\tau} d\tau \Phi,$$

T_s is sample period and k is the discrete sampling instant.

III. THEORETICAL ANALYSIS AND DESIGN OF THE PROPOSED CONTROL STRATEGY

The structure of the proposed strategy is depicted in Fig. 1, from which it can be observed that the control objectives can be met by the three cascaded control loops. The inner loop is to achieve active damping via full state-feedback using predicted state variables; the middle loop is utilized to combine the disturbance compensation and tracking performance together; whereas the outer loop is designed to improve the quality of grid-injected current by minimizing grid-injected current error online both in ideal and perturbed conditions.

A. STATE-FEEDBACK AND STATE OBSERVER

The full state-feedback is utilized in inner loop for the active damping, as described in Fig. 1. Accordingly, the control law is produced as:

$$u_i(k) = u_i^*(k) - K_v x(k) \tag{5}$$

where $u_i^*(k)$ denotes the output of the designed controller with disturbance compensation, and $K_v = \begin{bmatrix} k_1 & k_2 & k_3 \end{bmatrix}$ is the state-feedback gain vector.

Substituting (5) into (4) yields

$$\begin{cases} x(k+1) = (G - H_1K_v)x(k) + H_1u_i^*(k) + H_2u_g(k) \\ \qquad\qquad +\Gamma\lambda(k) \\ y(k) = C_cx(k). \end{cases} \tag{6}$$

Here, the analytical relationship from $u_i^*(k)$ to $i_g(k)$ is treated as a generalized controlled plant $P_G(z)$. Thus, from (6), the transfer function of the generalized plant is derived as

$$P_G(z) = C_c(zI_3 - G + H_1K_v)^{-1}H_1 \tag{7}$$

where I_3 is a three-dimensional identity matrix.

According to the guidelines for selecting the pole locations [30], [31], let the characteristic polynomial of (7) be

$$\det(zI_3 - G + H_1K_v) = (z-\alpha_1)(z-\alpha_2)(z-\alpha_3) \tag{8}$$

where α_1, α_2 and α_3 are the desired poles of the state-feedback, then the state-feedback gain vector K_v can be derived.

It should be noted that the full state-feedback requires more sensors compared with capacitor current feedback, which increases the system cost and vulnerability. Moreover, the computational delay has not been considered. In practice, however, one-step delay associated with the digital implementation exists between the control voltage and inverter output voltage. To account for the computational delay, the system dynamics is rewritten as follows

$$\begin{cases} x(k+1) = Gx(k) + H_1u_i(k-1) + H_2u_g(k) + \Gamma\lambda(k) \\ y(k) = C_cx(k). \end{cases} \tag{9}$$

Referring to [16], [32], an effective way to compensate for this time delay is to make one-step-ahead prediction of the state variables and utilize predicted states instead of the current states in determining the control law.

In order to reduce the number of sensors and predict state variables one-step ahead, a full-order state observer is utilized in this paper. Since the grid-injected current $i_g(k)$, PCC voltage $u_g(k)$ are measured and the inverter output voltage $u_i(k)$ is internally known, the remaining state variables can be estimated precisely, i.e.

$$\begin{cases} \hat{x}(k+1) = G\hat{x}(k) + H_1u_i(k-1) + H_2u_g(k) \\ \qquad\qquad +L[y(k) - \hat{y}(k)] \\ \hat{y}(k) = C_c\hat{x}(k) \end{cases} \tag{10}$$

where the subscript "$\hat{}$" denotes the estimated value, $L = \begin{bmatrix} l_1 & l_2 & l_3 \end{bmatrix}^T$ is the observer gain vector. With (9) and (10), the dynamics of the estimation error $e_x(k) = x(k) - \hat{x}(k)$ is

$$e_x(k+1) = (G - LC_c)e_x(k) + \Gamma\lambda(k). \tag{11}$$

According to the pole placement, the observer gain vector L can be determined, if the characteristic polynomial of the observer dynamics is selected as:

$$\det(zI_3 - G + LC_c) = (z-p_1)(z-p_2)(z-p_3) \tag{12}$$

where p_1, p_2, and p_3 are the desired poles of the state observer.

From (11), the estimation error will asymptotically converge under the elaborately selected poles, as long as the sufficient and necessary condition below is satisfied

$$\rho(G - LC_c) = \max_{1\le i\le 3} |\lambda_i(G - LC_c)| < 1 \tag{13}$$

where $\lambda_i(G - LC_c)$, $\rho(G - LC_c)$ denote the eigenvalues and spectral radius of G-LC_c, respectively.

Consequently, when the steady-state is reached, $e_x(k+1)$ and $e_x(k)$ will converge to the same, i.e.

$$\begin{aligned} \lim_{k\to\infty} |e_x(k+1)| &\approx \lim_{k\to\infty} |e_x(k)| \\ &\approx \lim_{k\to\infty} |(I_3 - G + LC_c)^{-1}\Gamma\lambda(k)|. \end{aligned} \tag{14}$$

It is obvious that there exists estimation error in the presence of lumped disturbance, which will inevitably degrade the control performance. Thus, aiming to improve the ability of disturbance rejection, a DOB is constructed.

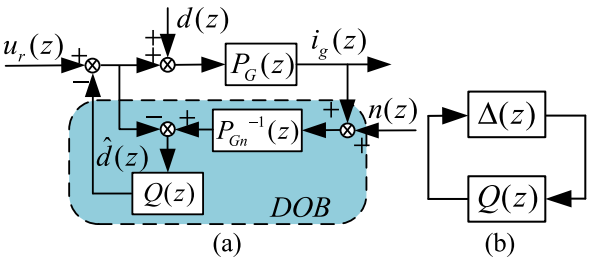

FIGURE 2. (a) Block diagram of DOB. (b) The standard M-Δ configuration of DOB for the small-gain theorem.

B. DISTURBANCE REJECTION BY DISTURBANCE OBSERVER

As mentioned above, the disturbance and model uncertainties may result in performance deterioration. For estimating and compensating this lumped disturbance, a DOB is designed, as depicted in Fig. 2. $u_r(z)$, $d(z)$, $\hat{d}(z)$ and $n(z)$ represent the controller output, external disturbance, estimated disturbance and measurement noise, respectively. $Q(z)$ is a low-pass filter which needs to be elaborately designed. $P_G(z)$ is the actual generalized plant defined by (7) and $P_{Gn}^{-1}(z)$ is the inverse of nominal generalized plant. To account for the mismatches between $P_G(z)$ and $P_{Gn}(z)$, $P_G(z)$ is formed into the output multiplicative perturbation description as follows

$$\begin{cases} P_G(z) = [1 + \Delta(z)]P_{Gn}(z) \\ \Delta(z) = W(z)\delta(z) \\ \|\delta(z)\|_\infty \le 1 \end{cases} \tag{15}$$

where $\Delta(z)$, $W(z)$, and $\delta(z)$ represent the modeling error, weighting function and variation, respectively.

Based on the block diagram in Fig. 2, the estimated disturbance can be derived as

$$\hat{d}(z) = \frac{Q(z)\Delta(z)u_r(z) + Q(z)\left[1+\Delta(z)\right]d(z) + Q(z)n(z)}{1+Q(z)\Delta(z)} \tag{16}$$

and the grid-injected current $i_g(z)$ is written as follows:

$$i_g(z) = G_{ri}(z)u_r(z) + G_{di}(z)d(z) + G_{ni}(z)n(z) \tag{17}$$

where $G_{ri}(z)$, $G_{di}(z)$, and $G_{ni}(z)$ denote the transfer functions from $u_r(z)$, $d(z)$, and $n(z)$ to $i_g(z)$, respectively. They are given by

$$\begin{cases} G_{ri}(z) = \dfrac{P_G(z)P_{Gn}(z)}{P_{Gn}(z) + Q(z)\left[P_G(z) - P_{Gn}(z)\right]} \\ \qquad\quad = \dfrac{\left[1+\Delta(z)\right]P_{Gn}(z)}{1+Q(z)\Delta(z)} \\ G_{di}(z) = \dfrac{\left[1-Q(z)\right]P_G(z)P_{Gn}(z)}{P_{Gn}(z) + Q(z)\left[P_G(z) - P_{Gn}(z)\right]} \\ \qquad\quad = \dfrac{\left[1-Q(z)\right]\left[1+\Delta(z)\right]P_{Gn}(z)}{1+Q(z)\Delta(z)} \\ G_{ni}(z) = -\dfrac{Q(z)P_G(z)}{P_{Gn}(z) + Q(z)\left[P_G(z) - P_{Gn}(z)\right]} \\ \qquad\quad = -\dfrac{Q(z)\left[1+\Delta(z)\right]}{1+Q(z)\Delta(z)}. \end{cases} \tag{18}$$

It is noted that the disturbance $d(z)$ is dominant in the low frequency segment, while the noise $n(z)$ is dominant in the high frequency segment. Thus, from (18), in the low frequency segment, $G_{di}(z) \approx 0$ provided that $Q(z) \approx 1$, which implies the disturbance can be effectively attenuated. Therefore, within the bandwidth of $Q(z)$, the grid-injected current $i_g(z)$ is deduced as

$$i_g(z) \approx P_{Gn}(z)u_r(z). \tag{19}$$

It can be seen from (19) that even if the actual plant is perturbed, the DOB forces it to maintain the characteristic of the nominal plant, which significantly improves the ability of disturbance rejection and relaxes the lumped disturbance sensitivity issue.

Then, we transfer the perturbed plant and DOB into the standard M−Δ configuration, as shown in Fig. 2(b). Based on the small-gain theorem [22], [25], the sufficient condition for the system stability can be easily obtained

$$\left\|\Delta(z)Q(z)\right\|_\infty < 1. \tag{20}$$

From (20), an improper $Q(z)$ would deteriorate the stability. Hence, when selecting the parameters of $Q(z)$, including the relative order and bandwidth, attention should be paid. In fact, the higher order of $Q(z)$ is, the faster response of the DOB becomes, but with the increasing order, phase lag may make the system unstable. On the other hand, a high bandwidth $Q(z)$ can enhance the anti-disturbance ability, however, it may easily result in system instability and increase the sensitivity to measurement noise $n(z)$. Thus, a tradeoff among the stability, disturbance suppression ability and noise sensitivity, must be made when designing DOB.

Considering that $P_G(z)$ is a three-order plant, to make $Q(z)P_{Gn}^{-1}(z)$ realizable, this paper defines $Q(z)$ as

$$Q(z) = \mathcal{Z}\left[\frac{1}{(\tau s+1)^3}\right] \tag{21}$$

where τ, $\mathcal{Z}[\cdot]$ denote the time constant and ZOH-transformation, respectively.

It can be obtained from (21) that $Q(z)$ is slightly less than unity within its bandwidth, which results in a fact that $G_{di}(z)$ is not strictly equal to zero. Therefore, the lumped disturbance cannot be completely eliminated and it will produce a transient component to the grid-injected current, which will degrade the dynamic performance. To further improve the quality of grid-injected current, an online adaptive control strategy with the self-learning ability is finally proposed.

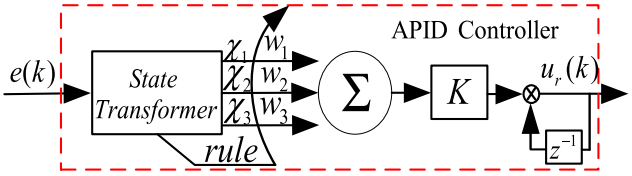

FIGURE 3. The schematic diagram of the APID controller.

C. ADAPTIVE PID CONTROLLER WITH THE SELF-LEARNING ABILITY

Fig. 3 shows the schematic diagram of the APID controller, where $e(k)$ is tracking error of grid-injected current at the k^{th} sampling instant, which is transformed into three internal variables, denoted χ_1, χ_2, and χ_3, respectively; w_1, w_2, and w_3 are the weight coefficients of the each internal variable; *rule* means the adaptive learning rule, which is utilized to adjust the weight coefficients online; K is the gain coefficient and $u_r(k)$ is the output of the APID controller.

The tracking error and internal variables are defined as follows:

$$\begin{cases} e(k) = i_{g,ref}(k) - i_g(k) - n(k) \\ \chi_1(k) = \Delta e(k) = e(k) - e(k-1) \\ \chi_2(k) = e(k) \\ \chi_3(k) = e(k) - 2e(k-1) + e(k-2). \end{cases} \tag{22}$$

Correspondingly, $u_r(k)$ can be expressed as

$$u_r(k) = u_r(k-1) + K\sum_{i=1}^{3} w_i(k)\chi_i(k). \tag{23}$$

Referring to optimal control theory, for pursuing excellent tracking performance, the quadratic performance index about $e(k)$ can be utilized. Thus, we insert a performance index function into the self-learning algorithm of the APID controller. The discrete-type quadratic error function is defined as

$$E(k) = \frac{1}{2}\left[i_{g,ref}(k) - i_g(k) - n(k)\right]^2 = \frac{1}{2}e(k)^2. \tag{24}$$

In order to minimize the error function $E(k)$, one can evaluate the following equation:

$$\frac{\partial E(k)}{\partial w_i(k)} = -e(k)\frac{\partial i_g(k)}{\partial u_r(k)}\frac{\partial u_r(k)}{\partial w_i(k)}, \quad i = 1, 2, 3. \tag{25}$$

For the steepest descent algorithm, the changes in weight coefficients can be deduced as

$$\begin{cases} \Delta w_1(k) = w_1(k) - w_1(k-1) = -\eta_P \dfrac{\partial E(k)}{\partial w_1(k)} \\ \qquad = \eta_P e(k)\dfrac{\partial i_g(k)}{\partial u_r(k)}\dfrac{\partial u_r(k)}{\partial w_1(k)} \\ \Delta w_2(k) = w_2(k) - w_2(k-1) = -\eta_I \dfrac{\partial E(k)}{\partial w_2(k)} \\ \qquad = \eta_I e(k)\dfrac{\partial i_g(k)}{\partial u_r(k)}\dfrac{\partial u_r(k)}{\partial w_2(k)} \\ \Delta w_3(k) = w_3(k) - w_3(k-1) = -\eta_D \dfrac{\partial E(k)}{\partial w_3(k)} \\ \qquad = \eta_D e(k)\dfrac{\partial i_g(k)}{\partial u_r(k)}\dfrac{\partial u_r(k)}{\partial w_3(k)} \end{cases} \tag{26}$$

where η_P, η_I, η_D are the proportional, the integral and the differential learning rates, respectively.

It can be observed from (23) that $\frac{\partial u_r(k)}{\partial w_i(k)}(i = 1, 2, 3)$ is equal to $K\chi_i(k)(i = 1, 2, 3)$. However, $\frac{\partial i_g(k)}{\partial u_r(k)}$ in (26) is uncertain. According to the engineering experience, when tuning the controller parameters, the $e(k)$ and $\Delta e(k)$ are expected to quickly converge to zero, which indicates the controller parameters tuning is associated with $e(k)$ and $\Delta e(k)$, so this paper utilizes $e(k) + \Delta e(k)$ to replace $\frac{\partial i_g(k)}{\partial u_r(k)}$. The calculation error can be compensated by the adjustable learning rates.

Therefore, the adaptive learning rule is rewritten as

$$\begin{cases} w_1(k) = w_1(k-1) + \eta_P K \chi_1(k) e(k)\left[e(k) + \Delta e(k)\right] \\ w_2(k) = w_2(k-1) + \eta_I K \chi_2(k) e(k)\left[e(k) + \Delta e(k)\right] \\ w_3(k) = w_3(k-1) + \eta_D K \chi_3(k) e(k)\left[e(k) + \Delta e(k)\right]. \end{cases} \tag{27}$$

Then, in order to ensure the convergence and robustness of (23) and (27), $w_i(k)(i = 1, 2, 3)$ is normalized as:

$$\bar{w}_i(k) = \frac{w_i(k)}{\sum_{j=1}^{3} \left|w_j(k)\right|}, \quad i = 1, 2, 3. \tag{28}$$

Accordingly, $u_r(k)$ in (23) can be modified as follows:

$$u_r(k) = u_r(k-1) + K\sum_{i=1}^{3} \bar{w}_i(k)\chi_i(k). \tag{29}$$

Expanding (29) and comparing with the incremental digital PID regulator, one can easily obtain the equivalent proportional gain K_P, the integral gain K_I and the differential gain K_D of the APID controller, i.e.

$$\begin{cases} K_P = K\bar{w}_1(k) \\ K_I = K\bar{w}_2(k) \\ K_D = K\bar{w}_3(k). \end{cases} \tag{30}$$

From the theoretical analysis above, the equivalent gains are able to be adjusted online to minimize grid-injected current error $e(k)$ and ensure robustness by the adaptive learning rule at each sampling instant. Hence, when the grid-injected current error occurs, caused by no matter the step-changed reference, parameters variation or disturbances, the performance index function $E(k)$ will be optimized, which will significantly improve the control performance.

In addition, the proposed adaptive strategy is designed with low computational burden. This strategy minimizes the requirements on the complexity and computational capacity. The relevant control parameters can be obtained by the trial-and-error method. And a rule of thumb to determine the values of K, η_P, η_I, and η_D is briefly summarized as follows:

1) Firstly, the values of initial weight coefficient $w_i(0)$ $(i = 1, 2, 3)$ can be set arbitrarily.
2) Then, the gain coefficient K needs to be elaborately selected. K can be adjusted by the experimental results. The response of system becomes fast as the value of K increases, but with the increasing value, the system may oscillate even become unstable.
3) Finally, determine the learning rates η_P, η_I, and η_D. They are tuned to balance the overshoot and settling time.

IV. ROBUSTNESS ANALYSIS BASED-ON THE SMALL-GAIN THEOREM UNDER MODEL UNCERTAINTIES

It should be pointed out that, in essence, the APID controller is a nonlinear incremental digital PID regulator with the self-learning ability. To evaluate the robustness, we simplify it as a linear one, denoted $C_e(z)$, whose equivalent gains are obtained under the nominal plant. This simplification for the purpose of analysis is feasible, since once the steady-state is reached, the APID controller will be converted as incremental digital PID regulator. While, during the transient-state, the APID controller has stronger adaptability due to the adjustable learning rule, which will achieve better performance than PID regulator. Hence, conclusions about the robustness drawn based-on PID regulator is also suitable for the APID controller.

In this section, the potential influence of parameter perturbation which may result in unexpected dynamics will be investigated. For simplification, the output multiplicative perturbation form in (15) is modified as follows:

$$P_G(z) = \left[1 + W(z)\delta(z)\right] P_{Gn}(z) \left\|\delta(z)\right\|_\infty \le 1. \tag{31}$$

Then, $W(z)$ can be derived for all frequency range as

$$\left|W(z)\right| \ge \left|\frac{P_G(z)}{P_{Gn}(z)} - 1\right|. \tag{32}$$

The inequality (32) implies that the frequency response curve of $W(z)$ is supposed to lie above the clustering frequency response curves of relative perturbation $[P_G(z)/P_{Gn}(z) - 1]$. Assuming that the filter parameters L_1, L_2 can drift $\pm 25\%$, C can drift $\pm 5\%$ around the nominal values [33] listed in Table 1, the clustering frequency response curves of $[P_G(z)/P_{Gn}(z) - 1]$ can be easily obtained, which are

TABLE 1. Parameters of the system.

Symbol	Description	Value
u_g	PCC voltage	110 V(RMS)
U_{dc}	DC link voltage	350 V
L_1	Inverter-side inductor	1.2 mH
L_2	Grid-side inductor	1.2 mH
C	Filter capacitor	6 μF
R_1	Equivalent series resistance of L_1	0.1 Ω
R_2	Equivalent series resistance of L_2	0.1 Ω
K_v	State-feedback gain vector	[13.1253 -0.3149 -3.1668]
L	State observer gain vector	[0.1463;-13.7063;0.5122]
K	Gain coefficient of APID	1.8
η_P,η_I,η_D	Learning rate	0.8, 0.1, 0.1
f_{sw}	Switching frequency	10 kHz
f_s	Sampling frequency	10 kHz

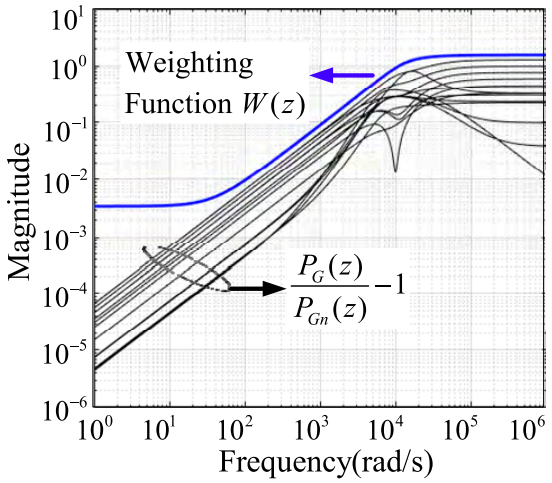

FIGURE 4. The frequency responses of the weighting function and relative perturbation.

depicted in Fig. 4. Taken the sufficient margins into consideration, a stable and minimum phase weighting function $W(z)$, which lies above the upper-bound frequency response curve, is selected as

$$W(z)=\frac{1.55z^3-2.1480z^2+0.6249z-0.0251}{z^3-0.6123z^2+0.1381z-0.0033}. \quad (33)$$

Then, we define the sensitivity transfer function $S(z)$ and complementary sensitivity transfer function $T(z)$:

$$\begin{cases} S(z)=\left[1+P_{Gn}(z)K_{eq}(z)\right]^{-1} \\ T(z)=1-S(z) \end{cases} \quad (34)$$

where $K_{eq}(z)$ is the equivalent controller on the standard feedback control structure and it is calculated as:

$$K_{eq}(z)=\frac{C_e(z)+Q(z)P_{Gn}(z)^{-1}}{1-Q(z)}. \quad (35)$$

Therefore, the robustness condition based on the small-gain theorem [22], [25] can be obtained

$$\|W(z)T(z)\|_\infty=\left\|W(z)\frac{P_{Gn}(z)K_{eq}(z)}{1+P_{Gn}(z)K_{eq}(z)}\right\|_\infty\le 1. \quad (36)$$

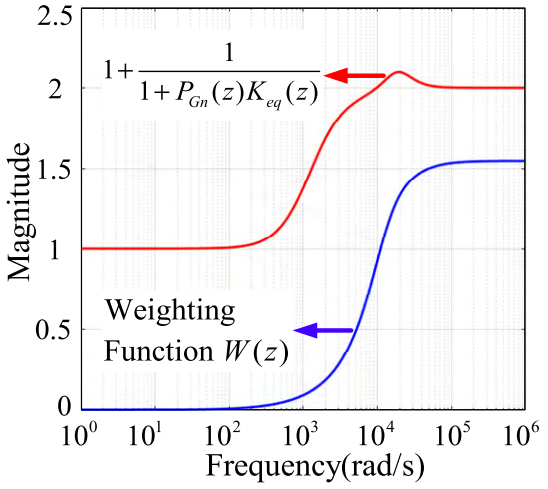

FIGURE 5. The robustness analysis based on the small-gain theorem.

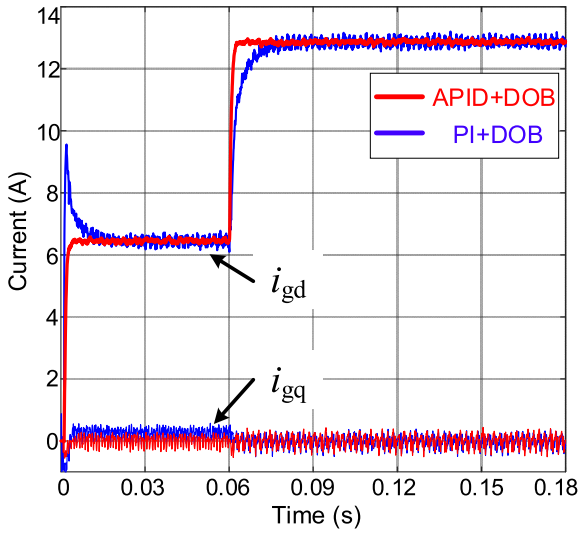

FIGURE 6. The transient responses of the grid-injected current in d- and q-axis under the step change in the active power and performance comparison between the APID + DOB and PI + DOB.

For simplicity, (36) can be transformed to

$$|W(z)|\le\left|1+\frac{1}{1+P_{Gn}(z)K_{eq}(z)}\right|. \quad (37)$$

From (37), the frequency response curve of $W(z)$ is expected to lie below the curve of the right-hand part. Both of them are depicted in Fig. 5. It is easily observed that the robustness under model uncertainties can be guaranteed.

V. SIMULATION AND EXPERIMENTAL VERIFICATION

A. SIMULATION VERIFICATION

In order to verify the effectiveness of the proposed strategy (APID + DOB), simulation tests on a 110 V/50 Hz/3 kW grid-connected inverter with *LCL* filter are carried out in MATLAB/Simulink environment based-on the system and current controller presented in Fig. 1, and the parameters utilized in simulations are listed in Table 1. In addition, to prove

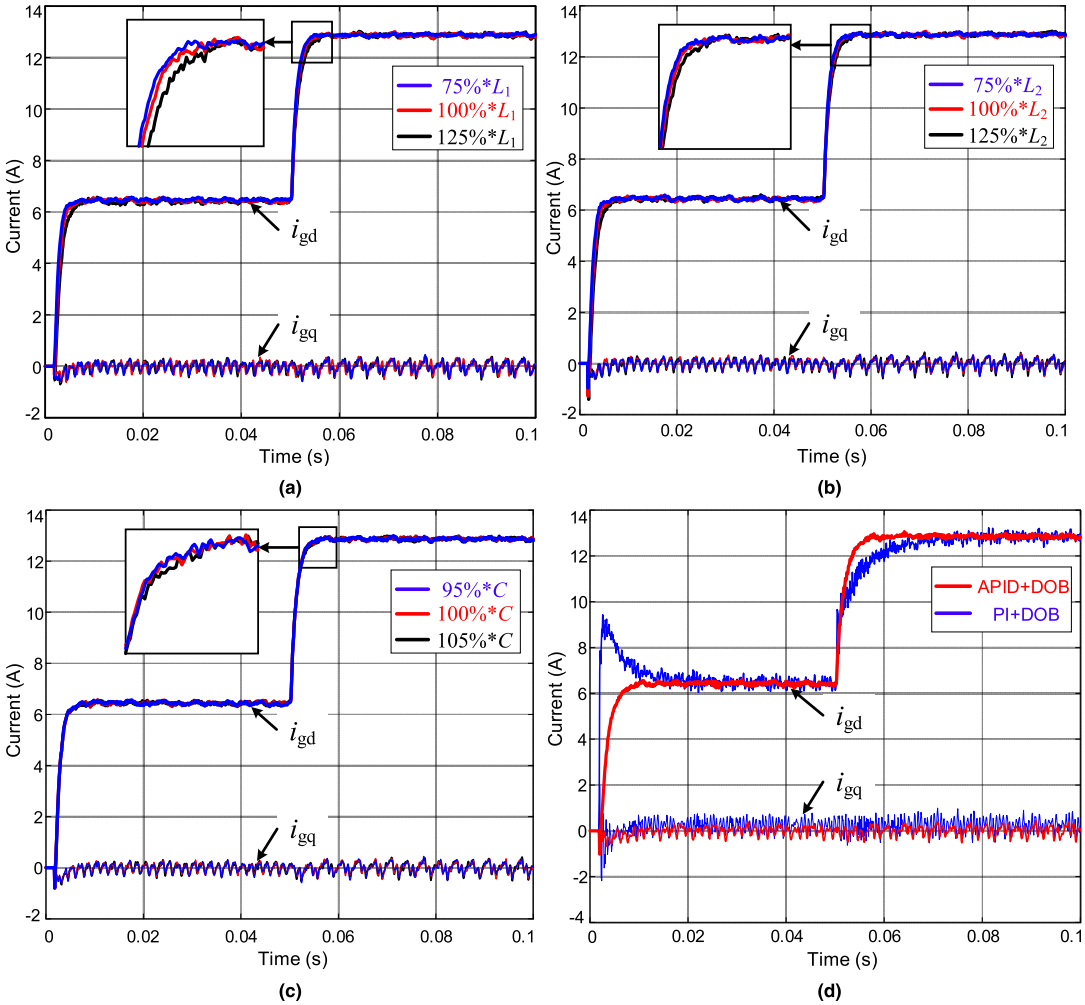

FIGURE 7. Robustness to the parameter uncertainties of the proposed strategy and performance comparison between the APID + DOB and PI + DOB when the filter parameters vary in a large range. (a) The transient responses under the APID + DOB when L_1 varies ±25% from the nominal value. (b) The transient responses under the APID + DOB when C varies ±5% from the nominal value. (c) The transient responses under the APID + DOB when L_2 varies ±25% from the nominal value. (d) The performance comparison between the APID + DOB and PI + DOB under the parameter variation of −25% in L_1, −5% in C and −25% in L_2.

more advantageous performances of the proposed strategy, the comparative studies with the conventional PI controller based on DOB (PI + DOB) are also conducted. And for a fair comparison, the optimal control parameters have been designed for PI + DOB.

1) TRANSIENT PERFORMANCE UNDER THE STEP CHANGE IN THE ACTIVE POWER

The objective of this simulation is to verify the transient performance and tracking ability of the grid-injected current under the proposed strategy. To this end, the q-axis current reference is set to zero, while the d-axis current reference is stepped up from 0 A to 6.43 A at t = 0 s, and then stepped up to 12.86 A at t = 0.06 s. The dynamic performances of the grid-injected current controlled by the APID + DOB and PI + DOB are shown in Fig. 6. It can be observed that the transient response without any overshoot under the APID + DOB is faster than that under PI + DOB. This can be explained as follows: when the reference is suddenly changed, the tracking error $e(k)$ occurs in the grid-injected current, and the discrete-type quadratic error function $E(k)$ defined in (24) will be optimized online by the steepest descent algorithm and self-learning rule. Therefore, the actual grid-injected current quickly converges to the reference and the error $e(k)$ asymptotically converges to zero. This confirms that the proposed strategy can achieve better transient performance and tracking ability compared with the traditional method.

2) ROBUSTNESS TO THE PARAMETER VARIATION

To evaluate the robustness to parametric variation of the proposed control strategy, a set of simulations under parameter mismatches have been carried out. Fig. 7(a)-(c) present the transient responses under the proposed strategy when L_1 varies ±25%, C varies ±5% and L_2 varies ±25% from the nominal values, respectively. It can be seen that,

compared with the transient performance under the nominal values, the dynamics almost keep unchanged regardless of the parameter variation. Thus the parameter variation in *LCL* filter brings little adverse effect on the grid-injected current under the proposed strategy, which sufficiently verifies the theoretical analysis in Section IV. In order to further highlight this advantage, the performance comparison between the APID + DOB and PI + DOB under parameter variation of -25% in L_1, -5% in C and -25% in L_2 is presented in Fig. 7(d). Clearly, during the transient state, the ripple is observed in the grid-injected current controlled by PI + DOB. Because the effect of the parameter uncertainties cannot be completely eliminated due to limitation of DOB, and it produces a transient component to grid-injected current, which degrades transient performance. This fully matches the theoretical analysis in Section III. While, it should be noted that the proposed strategy has overcome this issue, and it can remain the prominent performance under the severe parameter variation.

3) ADAPTABILITY FOR THE GRID INDUCTANCE VARIATION

This test is conducted to verify the ability of the proposed strategy to adapt the grid inductance variation. Fig. 8(a) and Fig. 8(b) depict the transient performances when the grid inductance varies from 0 mH to 4 mH under the PI + DOB and proposed strategy, respectively. In Fig. 8(a), the overshoot and oscillation are easily observed in the grid-injected current when the grid inductance increases. However, in Fig. 8(b), the proposed strategy can ensure fast convergence characteristics and precise tracking ability regardless of the grid inductance variation. As well known, the control bandwidth decreases as the grid inductance increases. The proposed strategy attenuates the influence of the grid inductance on the performance. This is due to the inherent self-tuning capability, which enables the controller to be redesigned in real time to achieve optimal performances. Thus the proposed strategy can achieve fast convergence properties with enough robustness and high control bandwidth.

4) ABILITY TO REJECT THE GRID DISTURBANCES

In this scenario, the effectiveness of the proposed strategy will be verified under the grid disturbances, such as the unbalanced grid voltage and the background harmonic voltage.

For a weak grid, the unbalanced grid condition commonly occurs due to the grid fault, highly unbalanced loads, etc. Fig. 9 depicts the simulated result of the grid-injected current under the unbalanced grid voltage which is emulated by 10% grid voltage sag in Phase B and 20% grid voltage sag in Phase C. From Fig. 9, it can be found that the grid-injected current has a perfect sinusoidal waveform with zero tracking error and low total harmonic distortion (THD), which demonstrates the ability of the disturbance rejection under the unbalanced grid voltage.

In addition, there may exist large amounts of the background harmonic voltage caused by the nonlinear loads in the grid. In order to further enhance the harmonic rejection ability, a harmonic compensator (HC regulator) [34] can be added in parallel with the APID controller to attenuate the grid-injected current distortions. Considering the

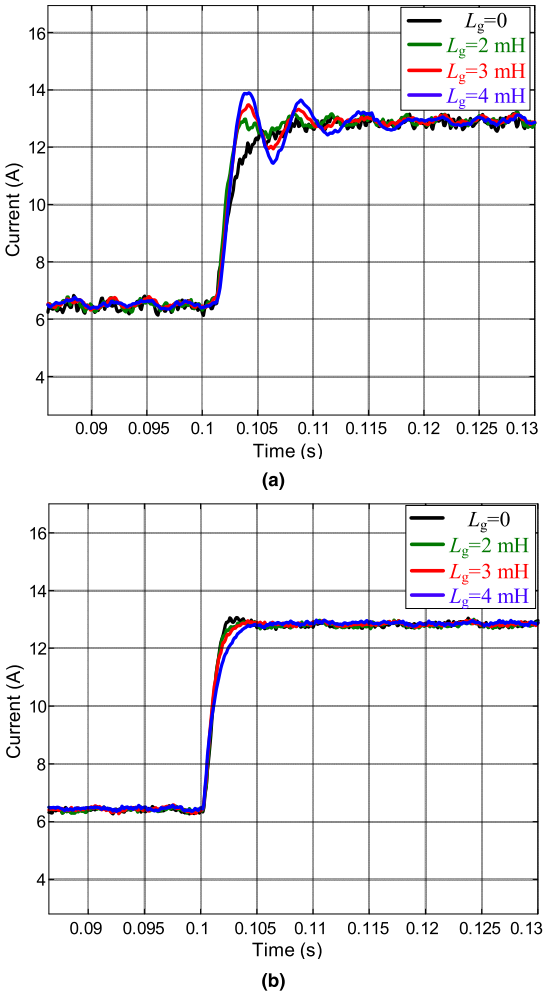

FIGURE 8. The transient performances when the grid inductance varies from 0 mH to 4 mH under the different control strategies. (a) PI + DOB. (b) APID + DOB.

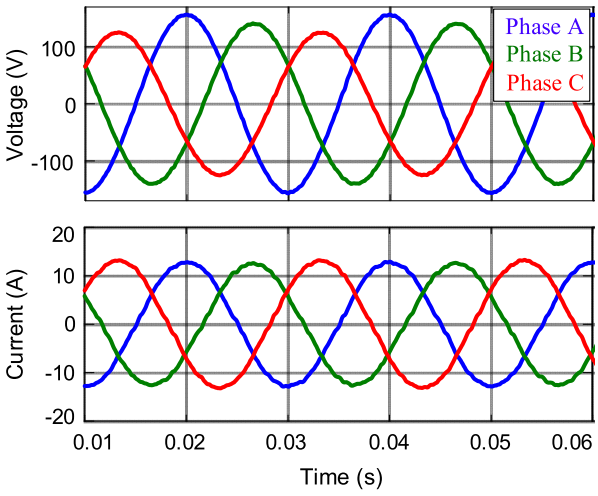

FIGURE 9. The simulated waveform of the grid-injected current under the unbalanced grid voltage.

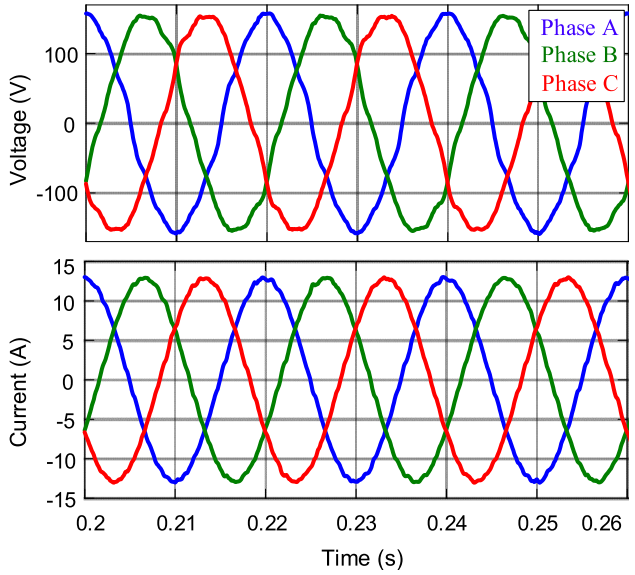

FIGURE 10. The simulated waveform of the grid-injected current under the distorted grid voltage.

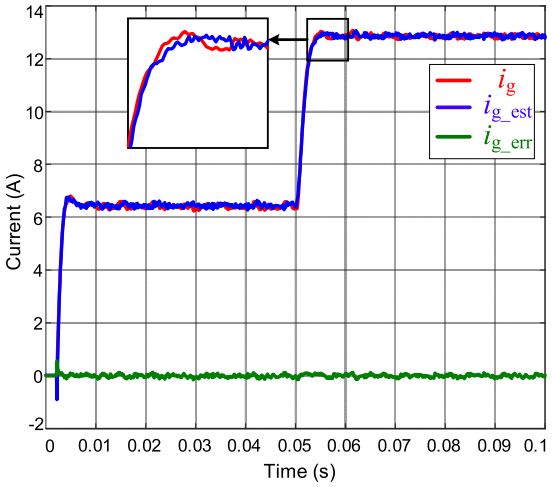

FIGURE 11. The simulated waveform of the measured grid-injected current and the estimated grid-injected current.

high bandwidth characteristics of the proposed strategy, an 11th HC regulator is utilized:

$$G_{hc}(z) = \mathcal{Z}\left[\sum_{h=2,4,6,8,10} \frac{K_h s}{s^2 + (\omega_g h)^2}\right] = \sum_{h=2,4,6,8,10} K_h \frac{\sin(\omega_g h T_s)}{2\omega_g h} \frac{z^2 - 1}{z^2 - 2z\cos(\omega_g h T_s) + 1} \tag{38}$$

where K_h denote the resonant gains and all of them are selected as 800 in this paper. Fig. 10 shows the simulated result of the grid-injected current under the grid voltage distorted by the 3rd 5th 7th 9th and 11th harmonics, whose magnitudes with respect to the grid fundamental voltage are

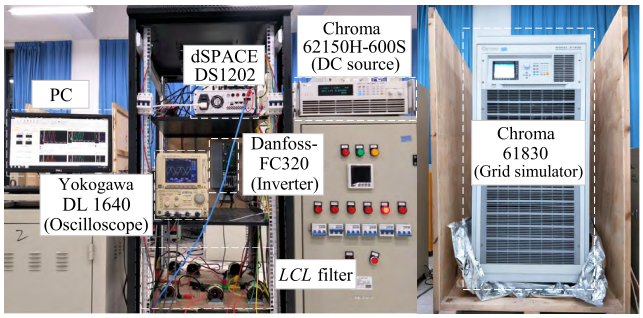

FIGURE 12. The experimental setup.

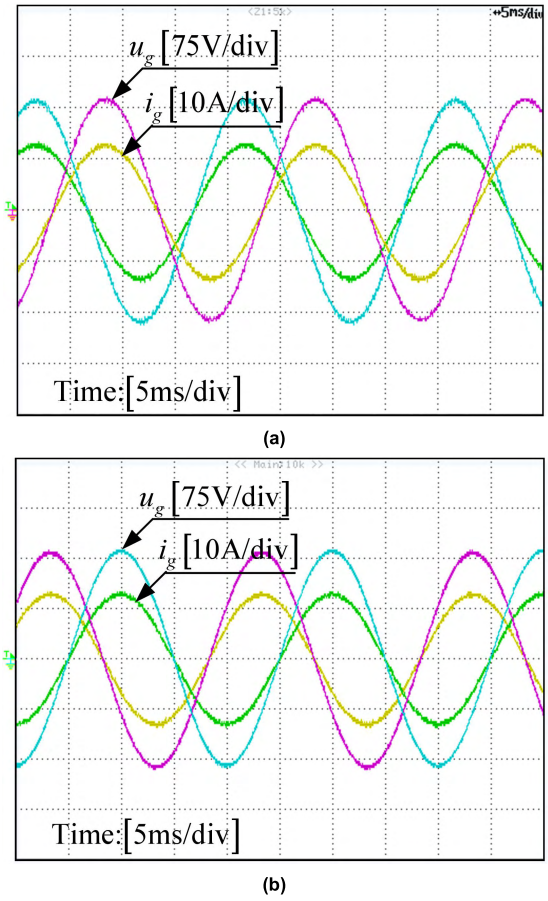

FIGURE 13. The steady-state experimental results under nominal power operation. (a) PI + DOB. (b) APID + DOB.

1.2%, 2.8%, 1.3%, 2.4%, and 1.5%, respectively. It can be seen that the grid-injected current remains sinusoidal waveform with zero steady-state error and low THD, which indicates that the proposed strategy can effectively reject up to 11th harmonic under the condition of $L_g = 4$ mH.

5) ACCURACY OF THE STATE VARIABLE ESTIMATED BY THE FULL-ORDER STATE OBSERVER

As analyzed in Section III, the accuracy of the state variables estimated by the full-order state observer affects the control performance. Fig. 11 presents the simulated waveform of the measured grid-injected current and the estimated

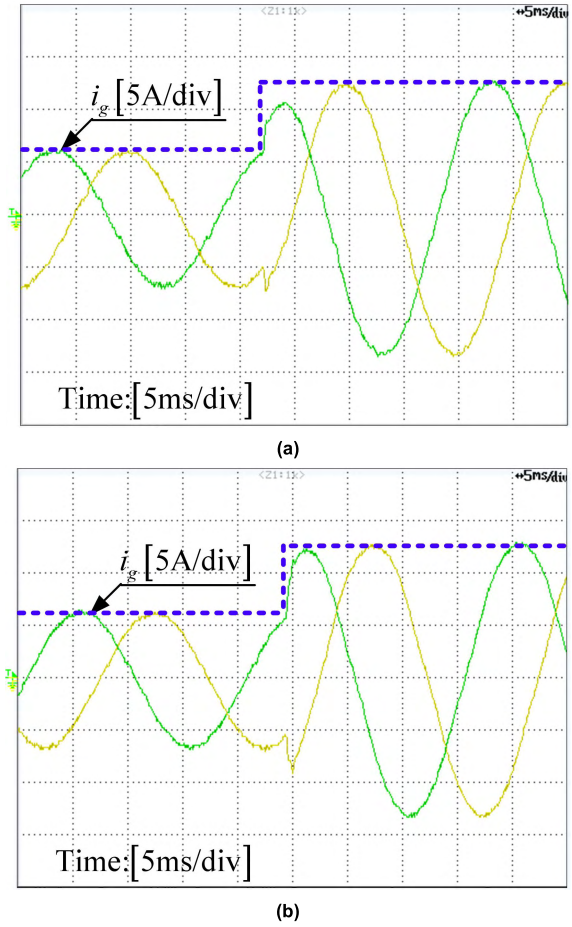

FIGURE 14. The dynamic waveforms of the grid-injected current under the step change in the active power. (a) PI + DOB. (b) APID + DOB.

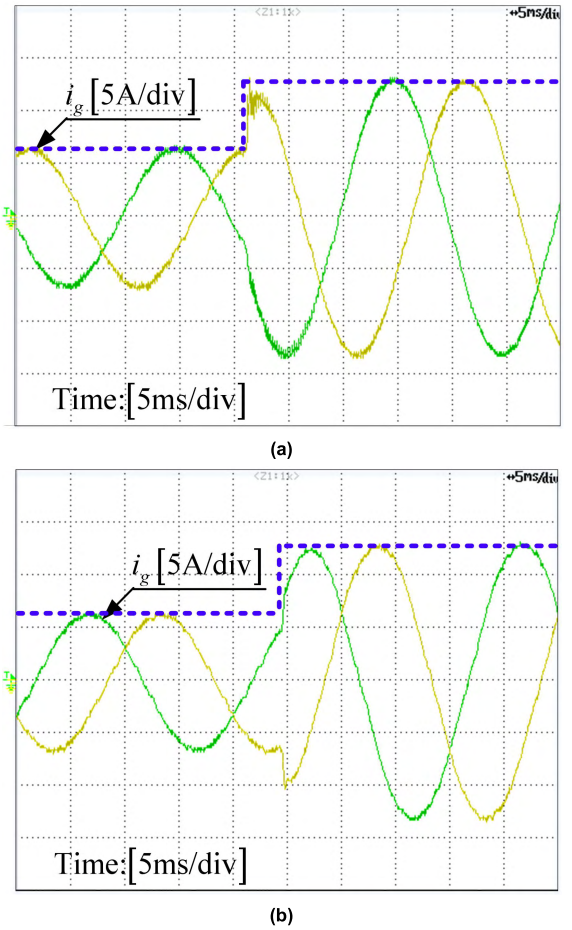

FIGURE 15. The dynamic performances under the parameter variation of −25% in L_1, −5% in C and −25% in L_2. (a) PI + DOB. (b) APID + DOB.

grid-injected current under a sudden change in the active power. In Fig. 11, i_g, i_{g_est} and i_{g_err} denote the measured grid-injected current, the estimated grid-injected current and the estimation error, respectively. It can be observed that the estimation is consistent with the measurement, and the estimation error is significantly small, which can be neglected. Thus, the high accuracy can be guaranteed. similarly, the remaining state variables i_1 and u_c can be precisely estimated, as well, which are omitted due to the length of this paper.

B. EXPERIMENTAL VERIFICATION

In order to further verify the theoretical analysis, a 110 V/ 50 Hz/3 kW prototype is constructed based on dSPACE DS1202, Danfoss-FC320, Chroma 61830 and Chroma 62150H-600S. The experimental setup is shown in Fig. 12 and the experimental parameters coincide with those utilized in simulations. To emulate the grid inductance, the external inductors are utilized. In addition, the comparative experiments based on PI + DOB are also carried out to highlight the superiority of the proposed strategy. And all the experimental waveforms are captured from a Yokogawa DL 1640 digital oscilloscope.

1) STEADY-STATE PERFORMANCE UNDER NOMINAL POWER OPERATION

In this scenario, the d-axis current reference is set to 12.86 A, while the q-axis current reference is set to zero. The corresponding steady-state performances under the PI + DOB and proposed strategy are shown in Fig. 13(a) and Fig. 13(b), respectively. It can be seen that both of them can achieve the zero steady-state error and unity power factor.

2) TRANSIENT RESPONSE UNDER THE STEP CHANGE IN THE ACTIVE POWER

The following experiments are performed to investigate the disturbance rejection performance and the dynamic response under a sudden change in the active power. Fig. 14 shows the dynamic waveforms of the grid-injected current when the q-axis current reference is kept equal to zero, while the d-axis current reference is suddenly stepped up from 6.43 A to 12.86 A. It can be easily observed from Fig. 14(a) that the transient response with settling time about 8 ms under PI + DOB is slower than the proposed strategy in Fig. 14(b). As shown in Fig. 14(b), the grid-injected current references are well tracked and the proposed scheme provides excellent

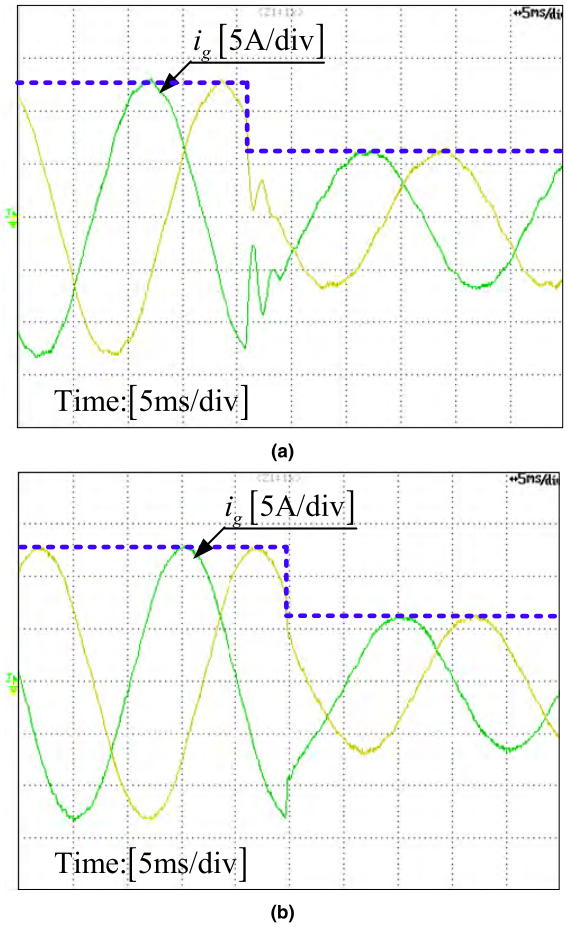

FIGURE 16. The dynamic performances when the grid inductance is 4 mH. (a) PI + DOB. (b) APID + DOB.

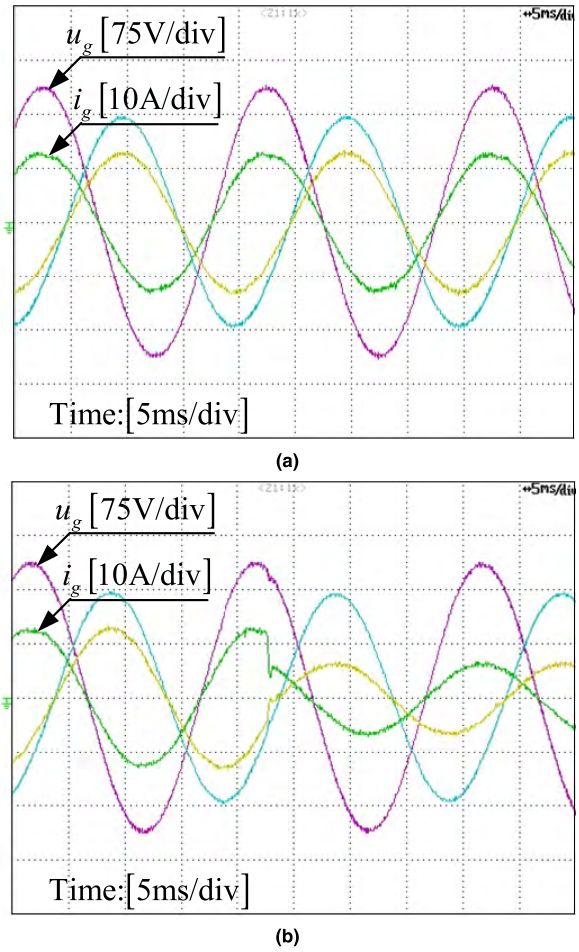

FIGURE 17. The experimental waveforms of the grid-injected current controlled by the proposed strategy under the unbalanced grid voltage. (a) The steady-state performance. (b) The transient performance.

dynamic performance with settling time about 3 ms and without overshoot. This also demonstrates the proposed strategy has stronger disturbance rejection capability under the sudden change in active power.

3) ROBUSTNESS TO THE PARAMETER VARIATION

These tests evaluate the robustness of the proposed method by investigating the sensitivity of the grid-injected current against the parameter uncertainties under a reference step-changed condition. To emulate the parameter uncertainties, the values of L_1, L_2, C are set with -25%, -25% and -5% variation from the nominal values. The dynamic performances with parameter uncertainties are shown in Fig. 15, revealing that the perturbed plant behaves as the same as the nominal plant during the steady state, regardless of the filtering deterioration due to the physical change of an *LCL* filter. That is because the DOB eliminates the influence of the parameter variation. However, the transient response under PI + DOB (with settling time about 7 ms in Fig. 15(a)) is still slower than that under the proposed strategy (with settling time about 3 ms in Fig. 15(b)). Especially, there are some current ripples in Fig. 15(a) during the transient state, which completely agrees with the simulation result, because the parameter variation as the internal disturbance defined in (3) results in the transient component superimposed on the grid-injected current. Compared with PI + DOB, the APID fully removes the ripple by optimizing the grid-injected current error, which is consistent with the theoretical analysis.

This simultaneously verifies the effectiveness and robust stability of the proposed strategy.

4) ADAPTABILITY FOR THE GRID INDUCTANCE VARIATION

In actual applications, the grid inductance may change in a large range. Thus, these experiments are performed to highlight the benefits of the proposed method to maintain the stability and fast dynamics in the presence of the grid inductance. To emulate the grid inductance, the external inductors ($L_g = 4$ mH) are adopted. Fig. 16 shows the dynamic performances when the d-axis current reference is stepped down from 12.86 A to 6.43 A. In Fig. 16(a), the oscillation can be easily observed under PI + DOB. In addition, the settling time and overshoot are up to 10 ms and 40%, respectively. The performance evidently deteriorates under the traditional method because the control bandwidth significantly reduces due to the great value of grid inductance. While, it can be

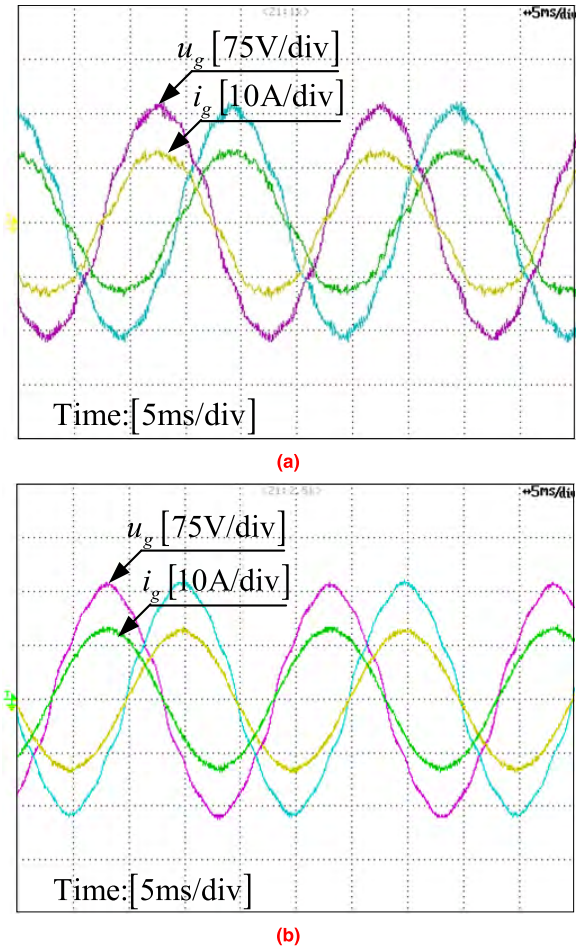

FIGURE 18. The experimental waveforms of the grid-injected current under the distorted grid voltage and $L_g = 4$ mH when HC regulator is adopted. (a) PI + DOB. (b) APID + DOB.

obtained from Fig. 16(b) that the fast transient performance against grid inductance variation is achieved with no oscillation and settling time about 4 ms. Different from the PI controller with fixed parameters, the APID can be automatically tuned online. Thus, the proposed strategy can achieve stronger adaptability and more prominent transient performance with high control bandwidth characteristics when the grid impedance varies widely.

5) ABILITY TO REJECT THE GRID DISTURBANCES

In applications, the grid-connected inverters are expected to normally operate no matter under the balanced grid condition or the unbalanced one. Fig. 17 depicts the experimental waveforms of the grid-injected current controlled by the proposed strategy under the unbalanced grid voltage. In Fig. 17(a), it is effectively demonstrated the ability to maintain the sinusoidal grid-injected current with zero tracking error even under the severely unbalanced grid condition. Simultaneously, Fig. 17(b) further reveals the prominent property of the fast performance recovery of the proposed strategy under the step change in the active power.

In order to further prove the ability of the proposed strategy to reject the grid disturbances, a programmable AC source (Chroma 61830) is utilized to emulate the grid voltage which is distorted by the 3rd, 5th, 7th, 9th and 11th harmonics. The magnitudes of harmonics with respect to the grid fundamental voltage are 1.2%, 2.8%, 1.3%, 2.4% and 1.5%, respectively. Fig. 18(a) depicts the experimental waveform of the grid-injected current under $L_g = 4$ mH, when an 11th HC regulator is in parallel with the PI controller. The THD of the grid-injected current is 4.7%. As a contrast, Fig. 18(b) depicts the experimental waveform of the grid-injected current under $L_g = 4$ mH, when an 11th HC regulator is in parallel with the APID controller. The THD is 1.8%, which is evidently lower than that under the traditional method. It can be seen that the grid-injected current maintains perfect sinusoidal waveform with low THD and the 11th harmonic has been successfully attenuated. These tests further verify that the proposed strategy can maintain the high-bandwidth characteristics under the great value of grid inductance and distorted grid voltage.

VI. CONCLUSION

In this paper, based on disturbance observer, an adaptive current control strategy with the self-learning ability is proposed to overcome the lumped disturbance sensitivity issue and improve the control performance. The principle of the proposed strategy is deduced in detail and the robust stability is analyzed based on the small-gain theorem. By theoretical analysis, the following conclusions can be drawn.

1) Embedding a DOB into control loop can effectively suppress the influence of disturbances and maintain the characteristic of the nominal plant, which significantly enhances the robust stability and ability of the disturbance rejection.
2) Optimizing the grid-injected current error through the steepest descent algorithm and self-learning rule, APID can achieve high control performance and tracking accuracy, even when the filter parameters and grid inductance vary widely.

Simulations and experiments on a 110 V/50 Hz/3 kW *LCL*-filter-based three-phase grid-connected inverter prototype verify the effectiveness of the proposed strategy.

REFERENCES

[1] W. Wu, Y. Liu, Y. He, H. S.-H. Chung, M. Liserre, and F. Blaabjerg, "Damping methods for resonances caused by *LCL*-filter-based current-controlled grid-tied power inverters: An overview," *IEEE Trans. Ind. Electron.*, vol. 64, no. 9, pp. 7402–7413, Sep. 2017.
[2] D. Yang, X. Ruan, and H. Wu, "A real-time computation method with dual sampling mode to improve the current control performance of the *LCL*-type grid-connected inverter," *IEEE Trans. Ind. Electron.*, vol. 62, no. 7, pp. 4563–4572, Jul. 2015.
[3] W. Wu, Y. He, and F. Blaabjerg, "An *LLCL* power filter for single-phase grid-tied inverter," *IEEE Trans. Power Electron.*, vol. 27, no. 2, pp. 782–789, Feb. 2012.
[4] R. Errouissi, A. Al-Durra, and S. M. Muyeen, "Design and implementation of a nonlinear PI predictive controller for a grid-tied photovoltaic inverter," *IEEE Trans. Ind. Electron.*, vol. 64, no. 2, pp. 1241–1250, Feb. 2017.

[5] M. B. Saïd-Romdhane, M. W. Naouar, I. Slama-Belkhodja, and E. Monmasson, "Robust active damping methods for *LCL* filter-based grid-connected converters," *IEEE Trans. Power Electron.*, vol. 32, no. 9, pp. 6739–6750, Sep. 2017.

[6] T. Hornik and Q.-C. Zhong, "A current-control strategy for voltage-source inverters in microgrids based on H^{∞} and repetitive control," *IEEE Trans. Power Electron.*, vol. 26, no. 3, pp. 943–952, Mar. 2011.

[7] D. Chen, J. Zhang, and Z. Qian, "An improved repetitive control scheme for grid-connected inverter with frequency-adaptive capability," *IEEE Trans. Ind. Electron.*, vol. 60, no. 2, pp. 814–823, Feb. 2013.

[8] X. Hao, X. Yang, T. Liu, L. Huang, and W. Chen, "A sliding-mode controller with multiresonant sliding surface for single-phase grid-connected VSI with an *LCL* filter," *IEEE Trans. Power Electron.*, vol. 28, no. 5, pp. 2259–2268, May 2013.

[9] R. P. Vieira, L. T. Martins, J. R. Massing, and M. Stefanello, "Sliding mode controller in a multiloop framework for a grid-connected VSI with *LCL* filter," *IEEE Trans. Ind. Electron.*, vol. 65, no. 6, pp. 4714–4723, Jun. 2018.

[10] Y. He, H. S.-H. Chung, C. N.-M. Ho, and W. Wu, "Use of boundary control with second-order switching surface to reduce the system order for deadbeat controller in grid-connected inverter," *IEEE Trans. Power Electron.*, vol. 31, no. 3, pp. 2638–2653, Mar. 2016,

[11] Y. He, H. S.-H. Chung, C. N.-M. Ho, and W. Wu, "Modified cascaded boundary-deadbeat control for a virtually-grounded three-Phase grid-connected inverter with *LCL* filter," *IEEE Trans. Power Electron.*, vol. 32, no. 10, pp. 8163–8180, Oct. 2017.

[12] N. Panten, N. Hoffmann, and F. W. Fuchs, "Finite control set model predictive current control for grid-connected voltage-source converters with *LCL* filters: A study based on different state feedbacks," *IEEE Trans. Power Electron.*, vol. 31, no. 7, pp. 5189–5200, Jul. 2016.

[13] S. Kwak and S. K. Mun, "Model predictive control methods to reduce common-mode voltage for three-phase voltage source inverters," *IEEE Trans. Power Electron.*, vol. 30, no. 9, pp. 5019–5035, Sep. 2015.

[14] Y. Liu, W. Wu, Y. He, Z. Lin, F. Blaabjerg, and H. S. H. Chung, "An efficient and robust hybrid damper for *LCL*- or *LLCL*-based grid-tied inverter with strong grid-side harmonic voltage effect rejection," *IEEE Trans. Ind. Electron.*, vol. 63, no. 2, pp. 926–936, Feb. 2016.

[15] W. Chen, J. Yang, L. Guo, and S. Li, "Disturbance-observer-based control and related methods-an overview," *IEEE Trans. Ind. Electron.*, vol. 63, no. 2, pp. 1083–1095, Feb. 2016.

[16] Y. Ye and Y. Xiong, "UDE-based current control strategy for *LCCL*-type grid-tied inverters," *IEEE Trans. Ind. Electron.*, vol. 65, no. 5, pp. 4061–4069, May 2018.

[17] B. Wang, Y. Xu, Z. Shen, J. Zou, C. Li, and H. Liu, "Current control of grid-connected inverter with *LCL* filter based on extended-state observer estimations using single sensor and achieving improved robust observation dynamics," *IEEE Trans. Ind. Electron.*, vol. 64, no. 7, pp. 5428–5439, Jul. 2017.

[18] A. Benrabah, D. Xu, and Z. Gao, "Active disturbance rejection control of *LCL*-filtered grid-connected inverter using Padé approximation," *IEEE Trans. Ind. Appl.*, vol. 54, no. 6, pp. 6179–6189, Nov./Dec. 2018.

[19] G. Lou, W. Gu, J. Wang, J. Wang, and B. Gu, "A unified control scheme based on a disturbance observer for seamless transition operation of inverter-interfaced distributed generation," *IEEE Trans. Smart Grid*, vol. 9, no. 5, pp. 5444–5454, Sep. 2018.

[20] J. Han, "From PID to active disturbance rejection control," *IEEE Trans. Ind. Electron.*, vol. 56, no. 3, pp. 900–906, Mar. 2009.

[21] M. Elkayam, S. Kolesnik, and A. Kuperman, "Guidelines to classical frequency-domain disturbance observer redesign for enhanced rejection of periodic uncertainties and disturbances," *IEEE Trans. Power Electron.*, vol. 34, no. 4, pp. 3986–3995, Apr. 2019.

[22] H. Muramatsu and S. Katsura, "An adaptive periodic-disturbance observer for periodic-disturbance suppression," *IEEE Trans. Ind. Informat.*, vol. 14, no. 10, pp. 4446–4456, Oct. 2018.

[23] J. Yang, W.-H. Chen, S. Li, L. Guo, and Y. Yan, "Disturbance/uncertainty estimation and attenuation techniques in PMSM drives—A survey," *IEEE Trans. Ind. Electron.*, vol. 64, no. 4, pp. 3273–3285, Apr. 2017.

[24] R. Errouissi and A. Al-Durra, "Design of PI controller together with active damping for grid-tied *LCL*-filter systems using disturbance-observer-based control approach," *IEEE Trans. Ind. Appl.*, vol. 54, no. 4, pp. 3820–3831, Jul./Aug. 2018.

[25] Y. Wu and Y. Ye, "Internal model-based disturbance observer with application to CVCF PWM inverter," *IEEE Trans. Ind. Electron.*, vol. 65, no. 7, pp. 5743–5753, Jul. 2018.

[26] H. T. Nguyen and J.-W. Jung, "Disturbance-rejection-based model predictive control: Flexible-mode design with a modulator for three-phase inverters," *IEEE Trans. Ind. Electron.*, vol. 65, no. 4, pp. 2893–2903, Apr. 2018.

[27] H. Yang, Y. Zhang, J. Liang, J. Liu, N. Zhang, and P. D. Walker, "Robust deadbeat predictive power control with a discrete-time disturbance observer for PWM rectifiers under unbalanced grid conditions," *IEEE Trans. Power Electron.*, vol. 34, no. 1, pp. 287–300, Jan. 2019.

[28] Y. Zhu and J. Fei, "Disturbance observer based fuzzy sliding mode control of PV grid connected inverter," *IEEE Access*, vol. 6, pp. 21202–21211, 2018.

[29] C. A. Busada, S. G. Jorge, and J. A. Solsona, "Full-state feedback Equivalent controller for active damping in *LCL*-filtered grid-connected inverters using a reduced number of sensors," *IEEE Trans. Ind. Electron.*, vol. 62, no. 10, pp. 5993–6002, Oct. 2015.

[30] J. Kukkola and M. Hinkkanen, "Observer-based state-space current control for a three-phase grid-connected converter equipped with an *LCL* filter," *IEEE Trans. Ind. Appl.*, vol. 50, no. 4, pp. 2700–2709, Jul./Aug. 2014.

[31] J. Kukkola, M. Hinkkanen, and K. Zenger, "Observer-based state-space current controller for a grid converter equipped with an *LCL* filter: Analytical method for direct discrete-time design," *IEEE Trans. Ind. Appl.*, vol. 51, no. 5, pp. 4079–4090, Sep./Oct. 2015.

[32] J. S. Lim, C. Park, J. Han, and Y. I. Lee, "Robust tracking control of a three-phase DC-AC inverter for UPS applications," *IEEE Trans. Ind. Electron.*, vol. 61, no. 8, pp. 4142–4151, Aug. 2014.

[33] Z. Zhang, W. Wu, Z. Shuai, X. Wang, A. Luo, H. S.-H. Chung, and F. Blaabjerg "Principle and robust impedance-based design of grid-tied inverter with *LLCL*-filter under wide variation of grid-reactance," *IEEE Trans. Power Electron.*, vol. 34, no. 5, pp. 4362–4374, May 2019.

[34] Y. Tang, P. C. Loh, P. Wang, F. H. Choo, and F. Gao, "Exploring inherent damping characteristic of *LCL*-filters for three-phase grid-connected voltage source inverters," *IEEE Trans. Power Electron.*, vol. 27, no. 3, pp. 1433–1443, Mar. 2012.

JIAHAO LIU was born in Henan, China, in 1993. He received the B.S. degree in electrical engineering from the Henan University of Science and Technology, Henan, China, in 2017. He is currently pursuing the M.S. degree in electrical engineering from Shanghai Maritime University, Shanghai, China.

His current research interests include digital control techniques of power converters and renewable energy generation system.

WEIMIN WU (M'16) received the Ph.D. degree in electrical engineering from the College of Electrical Engineering, Zhejiang University, Hangzhou, China, in 2005.

He was a Research Engineer with the Delta Power Electronic Center (DPEC), Shanghai, from July 2005 to June 2006. Since July 2006, he has been a Faculty Member at Shanghai Maritime University, where he is currently a Full Professor with the Department of Electrical Engineering. He was a Visiting Professor with the Center for Power Electronics Systems (CPES), Virginia Polytechnic Institute and State University, Blacksburg, VA, USA, from September 2008 to March 2009. From November 2011 to January 2014, he was also a Visiting Professor with the Department of Energy Technology, Aalborg University, Demark, working at the Center of Reliable Power Electronics (CORPE). He has coauthored over 100 papers and holds eight patents. His areas of interests include power converters for renewable energy systems, power quality, smart grid, and energy storage technology. He serves as an Associate Editor for the IEEE TRANSACTIONS ON INDUSTRY ELECTRONICS.

HENRY SHU-HUNG CHUNG (M'95–SM'03–F'16) received the B.Eng. and Ph.D. degrees in electrical engineering from the Hong Kong Polytechnic University, Hong Kong, in 1991 and 1994, respectively. Since 1995, he has been with the City University of Hong Kong, Hong Kong, where he is currently a Professor with the Department of Electronic Engineering, and the Director of the Center for Smart Energy Conversion and Utilization Research. His current research interests include renewable energy conversion technologies, lighting technologies, smart grid technologies, and computational intelligence for power electronic systems. He has edited 1 book, authored 8 research book chapters, and over 400 technical papers, including 180 refereed journal papers in his research areas, and holds 47 patents. He was the Chair of the Technical Committee of the High-Performance and Emerging Technologies, the IEEE Power Electronics Society (2010–2014). He has received numerous industrial awards for his invented energy-saving technologies. He is currently the Editor-in-Chief of the IEEE Power Electronics Letters and an Associate Editor of the IEEE Transactions on Power Electronics and the IEEE Journal of Emerging and Selected Topics in Power Electronics.

FREDE BLAABJERG (S'86–M'88–SM'97–F'03) was with ABB-Scandia, Randers, Denmark, from 1987 to 1988. From 1988 to 1992, he was a Ph.D. student in electrical engineering with Aalborg University, Aalborg, Denmark. He became an Assistant Professor (1992), an Associate Professor (1996), and a Full Professor of power electronics and drives (1998). Since 2017, he has been a Villum Investigator. His current research interests include power electronics and its applications such as in wind turbines, PV systems, reliability, harmonics, and adjustable speed drives. He has published more than 450 journal papers in the fields of power electronics and its applications. He is the coauthor of two monographs and the editor of six books in power electronics and its applications. He was the Editor-in-Chief of the IEEE Transactions on Power Electronics, from 2006 to 2012.